Current density imaging by pulsed conduction electron spin resonance

Malte Drescher [a,*], Noam Kaplan [b], Elmar Dormann [a]

[a] *Physikalisches Institut, Universität Karlsruhe (TH), D-76128 Karlsruhe, Germany*
[b] *Racah Institute of Physics, Hebrew University of Jerusalem, 91904 Jerusalem, Israel*

Abstract

In analogy with Nuclear MRI, the ESR signal phase shift of conduction electrons moving in electrical currents along controlled magnetic field gradients can be used to generate spatial *electronic current* density maps. First two-dimensional images of the current density distribution in quasi-one-dimensional organic conductors are presented.
© 2006 Elsevier Inc. All rights reserved.

1. Introduction

Electron-Spin magnetic resonance imaging (ESMRI) is conceptually almost identical with nuclear magnetic resonance imaging (NMRI) in that they both involve the detection of spins in magnetic field gradients. Due to the comparatively fast electron spin relaxation times, ESMRI is technically demanding and therefore much less developed. Nevertheless, a variety of experimental schemes have been already adapted from NMRI and the number of applications appears to be growing steadily [1–4]. Thus, focussing on *conduction* electrons in particular, some recent studies used ESMRI to investigate the statistical electron motion, i.e. electronic diffusion (see for example [5,6]). In these cases, the locally mapped spin echo time-decay under applied gradients was investigated.

In connection with one of the most important manifestations of conduction electrons—namely electrical current—further analogy to NMRI comes to mind: Using phase contrast NMRI to measure material flow is a well-known practice developed extensively for noninvasive quantitative imaging of *in vivo* blood flow, yielding many of the clinical procedures of MRI angiography [7,8]. The basic principle [9,10] involves monitoring the phase shift of nuclear spins attached to molecules that move with the liquid along a magnetic field gradient in combination with spatial resolution obtained by standard imaging techniques. In this work, we present the adaption of the phase-contrast method to conduction electrons in order to visualize *electrical current density* distribution in solids.

2. Experimental details

2.1. Imaging scheme

For an introduction to NMRI, we refer to standard textbooks [11,12]. The principles of scanning $\vec{k}$-space [13]

$$\vec{k} = \frac{1}{2\pi}\gamma \int \vec{G}(t)\,\mathrm{d}t \qquad (1)$$

(with gyromagnetic ratio γ and applied magnetic field gradient $\vec{G}$), known from NMRI, can be directly adapted to electron spin resonance imaging. Scanning the k-space in a cartesian grid and deriving spin density images by performing inverse Fourier transforms is the well-known so called Fourier Imaging.

---
* Corresponding author.
 E-mail address: malte.drescher@pi.uka.de (M. Drescher).

In order to detect the conduction electron flow resulting from (or leading to) a constant dc current I, we use a modification of a basic flow-encoding building block [11]. Beside the standard spin echo excitation sequence $\pi/2$–τ–π–τ-echo and a set of phase encoding gradients with variable strength to implement the Fourier Imaging, this sequence contains a quasi-static gradient which is constant at least during the whole excitation-acquisition period, starting at $t < 0$ and ending at $t > 2\tau$. Such quasi-static gradient is depicted as G_x on the left hand side in Fig. 1. Assuming stationary spins, the quasi-static gradient effects a dephasing during the first part of the sequence which is compensated by the same gradient after applying the refocusing π-pulse, leaving the phase of the signal at the center of the spin echo, at 2τ, unchanged. But in the presence of a DC electronic current, with the spins acquiring a constant component of velocity along the gradient direction x, the position of the electron spins and therewith the spatially depending magnetic field strength as well as their Larmor frequency vary with time, resulting in a phase shift of the central echo signal given by

$$\Delta\phi(2\tau) = -\gamma G v \tau^2. \tag{2}$$

Using Eq. (2) for $\Delta\phi$ leads to a systematic error, as it is accurate for the scheme depicted in Fig. 1 only in the limit of vanishing width for the $\pi/2$ and π RF pulses. An accurate expression can be easily derived for the more common 'modified bipolar' scheme with finite RF pulse-widths, provided G_x is kept off for the duration of the RF pulses [11]. However, the benefit of thus eliminating the small systematic error in $\Delta\phi$ is more than compensated by the technical simplification and the increased sensitivity offered by the sequence of Fig. 1.

It should be noted that the quasi-static gradient G_x is not used, in this case, as a classic read gradient to obtain spatial resolution, but rather as a phase encoding gradient. Thus, only the $t = 2\tau$-data point is analyzed. A crucial point in the practice of detecting *electrical* currents by

phase contrast experiments arises because of the additional magnetic field gradients generated by the current itself. To eliminate these additional gradients, a difference experiment was developed. The experiment is repeated twice, once with G_x and another time with inverted gradient polarity $-G_x$. In both experiments, a phase shift, $\Delta\phi^+$ or $\Delta\phi^-$, respectively, is detected (Fig. 1). Because the current induced magnetic field gradients are unchanged by the inverted G_x gradient, their influence on the phase shift is annulled by subtracting the signals of both experiments. Thus corrected, the phase shift can be written as

$$\Delta\Phi = \Delta\phi^+(2\tau) - \Delta\phi^-(2\tau) = -2\gamma G v \tau^2 \tag{3}$$

choosing $\Delta\Phi \equiv 0$ for $I = 0$.

2.2. Experimental realization

Detecting the small phase shifts expected and found in our case dictates a S/N ratio which is attainable only by performing the pulsed ESR in the microwave frequency range rather than in the lower radio-frequency range available in standard NMR imagers. The pulsed ESR imaging results were obtained with a commercial Bruker Elexsys E580 spectrometer at approximately 9.3 GHz, using an ER 4118X-MD4 dielectric ring resonator installed inside an ER4118CF continuous flow cryostat. For the experiments described below, liquid nitrogen was used as cooling agent. The $\pi/2$–τ–π–τ-echo pulse sequence was applied with a typical length of 16 ns for the $\pi/2$-pulse and using a 16-step phase cycle [11]. Hall probe regulation of the magnetic field strength of the electromagnet, cooled via heat exchanger, provided sufficient long-time stability.

The standard Bruker set-up has been equipped additionally with a home-built three-dimensional gradient system to generate the pulse sequence described above, as well as a special sample holder used to provide the electrical current through contacted samples inside the cavity. We use a coordinate system defined by the horizontal polarizing external field (z), the vertical cavity access axis (y) and the third perpendicular direction (x). A quadrupolar gradient coil, mounted around the adapted outer shell of the cryostat, enables the application of quasi-static gradients in the x-direction reaching $G_x \leqslant 0.2$ T/m for periods of at least 2 ms. To obtain the required short gradient pulses at the sample position, both G_y and G_z had to be realized with coils situated inside the dielectric ring resonator. The pulsed G_z-gradient is generated by Anti-Helmholtz gradient coils developed and delivered by Bruker, and inserted inside the ER 4118X-MD4 dielectric ring resonator. The gradient intensity amounts to $G_z/I_{G_z} = 0.66$ T/m/A. The pulsed gradient G_y is implemented with a pair of "8" shaped 0.1 mm thick copper loops of about 7 mm total extension (Fig. 2), fixed with two component epoxy resin between two 50 μm thick plastic films and introduced into the inner bore of the G_z-coils after being bent into cylindrical form. The coils are situated more than 5 mm apart from the metallic walls of the cavity [11,14].
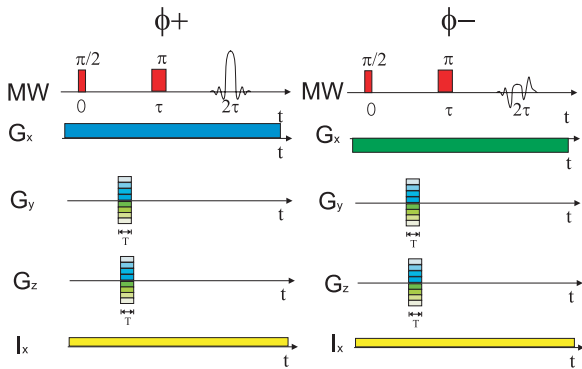

Fig. 1. Schematic of the pulse sequence containing pulsed Fourier imaging gradients $G_{y,z}$ as well as a "static" gradient G_x resulting in a current induced phase shift. $G_{y,z}$ were stepped in both polarities to scan data points in two-dimensions of k-space. Two experiments, ϕ^+ and ϕ^-, with inverted current encoding gradient are performed in order to eliminate additional, unwanted current induced gradients. The spin echo phase shift was determined at $t = 2\tau$.
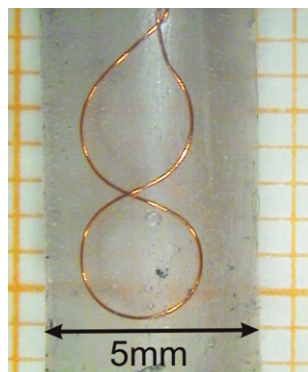
Fig. 2. Photography of the "8" shaped gradient coils producing G_y.

The gradient pulses were produced with pulse drivers based on the "clipped L–C resonant circuit" idea [15,16] allowing to apply short gradients ($T \approx 1\,\mu s$) of sufficient strength. As the gradient pulses G_y and G_z must fit into the Hahn spin echo pulse separation time τ in our experimental set-up, a lower limit of $\tau \geqslant 2\,\mu s$ is dictated for our experimental sequence (Fig. 1).

Having a well-controlled fast switching pulsed gradient system is a crucial requirement for this novel experiment. Therefore, we present in Fig. 3 an overview of the experimentally realized time dependencies of the various gradients and current pulses. Controlling and timing of the current, microwave, and gradient pulse channels is done by Bruker E585-PDCH Pattern Jet boards.

Technical limitations, effecting the pulsing capabilities of our ESMRI setup, dictated our preference to investigate solid conductors with transverse conduction-electron spin relaxation times $T_2 \geqslant 3\,\mu s$. The system chosen for the present experiment is the radical cation salt (fluoranthene)$_2$PF$_6$ [(FA)$_2$PF$_6$]. It is an organic conductor which is an almost ideal candidate for the application of magnetic resonance techniques, featuring a narrow ESR-line with typical values of $T_1 \approx T_2 \approx 8\,\mu s$ due to the weak spin–orbit coupling and spin–spin-interaction of the charge carriers. (FA)$_2$PF$_6$ proved already to be suitable for ESMRI, obtaining a resolution of down to 10 µm [17]. An example of three-dimensional results of ESR-imaging on (FA)$_2$PF$_6$ can be seen also on the cover of volume 180(2) of this journal [14].

Due to its special crystal structure, (FA)$_2$PF$_6$ acts as a quasi-one-dimensional conductor, and the related highly anisotropic diffusion coefficient D has been also determined quite early by pulsed magnetic resonance techniques [18,19]. Because the intrinsic anisotropy of the spin diffusion coefficient D and the charge carrier mobility μ is larger than 10^4:1 in (FA)$_2$PF$_6$, spatial restriction of the charge and spin carriers due to interruptions of the individual one-dimensional FA stacks can give rise to highly reduced effective values of $D_\parallel$ and $\mu_\parallel$ (factor of 50 [21]). Whereas the spatially varying, but low density of defects barely influences the conduction electron spin density in the metallic phase, it modulates the conduction electron relaxation rates and mobility and causes inhomogeneous current dis-
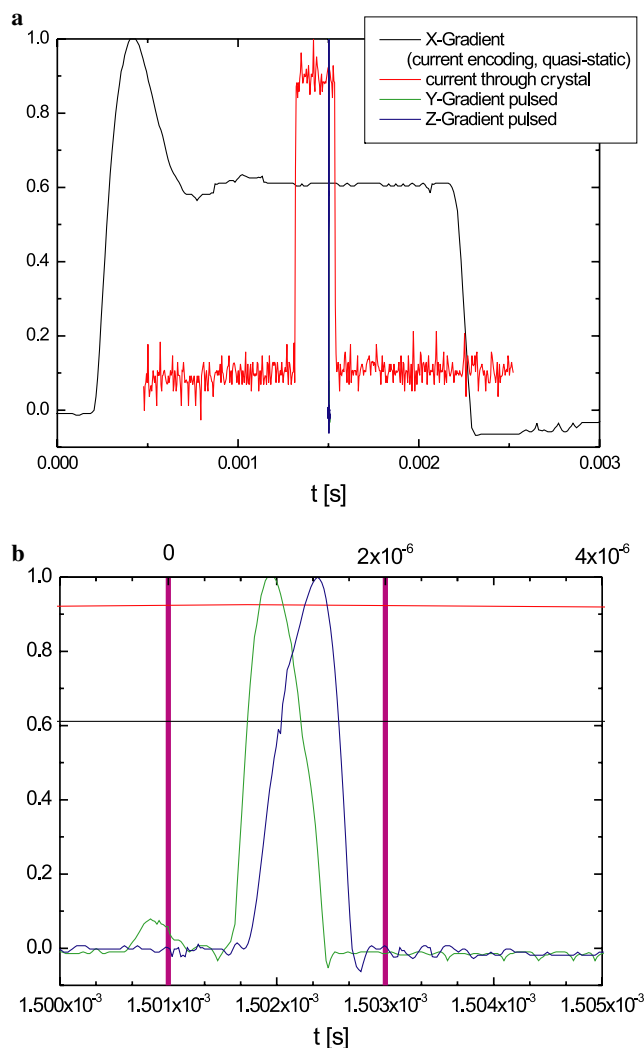

Fig. 3. Original experimental data of the three-dimensional gradient set-up and the current applied through the contacted sample. (a) The velocity encoding gradient G_x is applied for a period of about 2 ms and the current itself is applied for a period of 200 µs. Both can be called quasi-statically compared to the much shorter period of the Hahn spin-echo sequence ($2\tau \simeq 4\,\mu s$). (b) Increasing the time resolution, the shape and positions of the $G_{y,z}$ gradient pulses are shown related to the absolute timing of the Hahn sequence (upper scale, $t \equiv 0$ for the $\pi/2$ RF pulse). Note that the applied sample current as well as the velocity encoding gradient can be assumed constant during this period.

tribution of a crystal contacted at both ends. The uninterrupted conducting FA stacks—in the 1% range for typical (FA)$_2$PF$_6$ crystals [5,23]—predominate in the electrical current. In the present context, the quasi-one-dimensional behavior helps to minimize yet another possible complication caused by the existence of Hall forces expected to influence the motion of the moving charge carriers in magnetic fields.

According to Eq. 3, increasing the motion encoding gradient and the pulse separation time leads directly to enhanced phase shift. Nevertheless, in addition to the gradient-independent spin–spin relaxation T_2, a gradient dependent signal decay due to electron-spin diffusion, with

$\exp(-\frac{2}{3}D\gamma^2 G^2\tau^3)$ [20], must also be considered. Assuming $D \approx 2\,\frac{cm^2}{s}$ [21], the experimental sequence parameters were optimized by choosing $\tau = 2\,\mu s$ and $G_x = 0.1\,\frac{T}{m}$.

The difference method, used to eliminate unwanted gradients caused by the current itself, requires improved reproducibility of the applied gradients and the current distribution in the cavity. Thus, vibrations were minimized by conducting the current through a pair of rigid copper strips placed on an elongated printed circuit (pc) board instead of using wires. The pc board width is restricted by the inner diameter of the gradient coils to $d \approx 2\,mm$. The contact itself is made by short gold wires (diameter $25\,\mu m$) glued by graphite paint on the surface of the crystal. The contacts were stable for several days in nitrogen atmosphere featuring typical total (contact and intrinsic) resistances of about $R \approx 32\,\Omega$. The experiments were performed at $T = 250\,K$ to minimize heating of the gradient coils and of the sample by the applied current but still staying in the metallic phase above the Peierls transition temperature ($T_P \approx 186\,K$ [22]) and reaching the optimum of T_2 and χ [21] as well.

A special sample arrangement, consisting of two $(FA)_2PF_6$ crystals, was prepared to enable calibration tests as well as actual measurements. One rod-shaped crystal, $1.4\,mm \times \sim 0.4\,mm$, with conduction direction along the rod axis, is placed in the center of the y,z imaging field of view determined by $G_{y,z}$, with the highly conductive axis along the x-direction. The surfaces at both ends of the rod are contacted with glued gold wires. Another somewhat smaller size crystal is mounted of-center on the
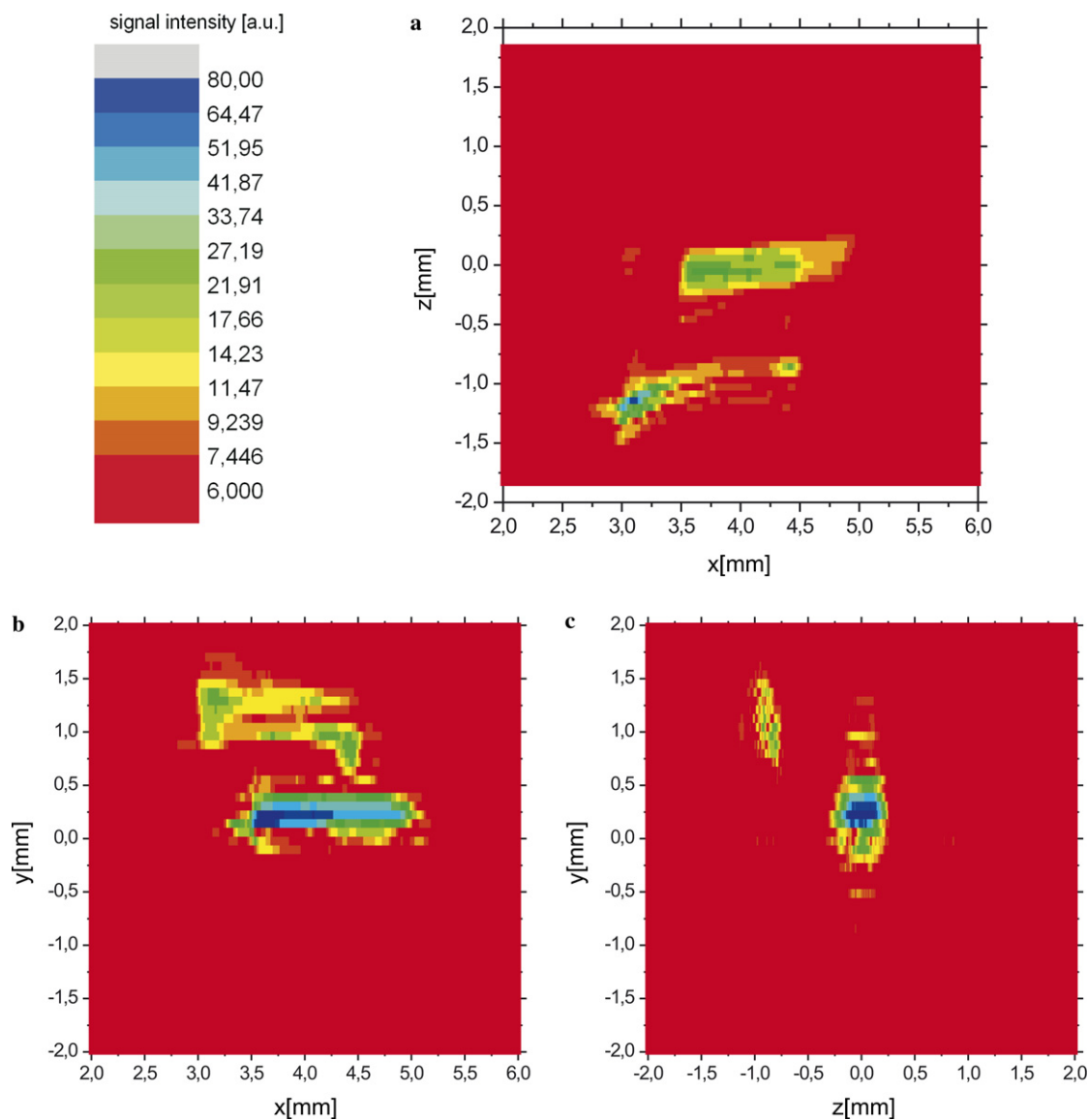

Fig. 4. ESR-images of the sample arrangement of two $(FA)_2PF_6$-crystals. Spatially resolved, T_2 weighted conduction electron spin density is displayed in three two-dimensional projections perpendicular to each other. The crystal centered around (4 mm, 0, 0) is as planned oriented with highly conductive axis parallel to x-direction which is also the direction of the applied current and the current encoding gradient G_x. Approximate pixel size horizontal (vertical) [μm]: (a) 22 (57), (b) 22 (82), (c) 3(82).

opposite side of the pc board and is used as a reference probe. This second crystal is not contacted electrically.

3. Experimental results and discussion

3.1. Three-dimensional spin density imaging

The three-dimensional spatially resolved, T_2 weighted conduction electron spin density (or better magnetization, because both are non-trivially related in a one-dimensional metal with Pauli-paramagnetism modified by charge density wave fluctuations announcing the Peierls transition towards a low-temperature non-metallic state!) is shown in Fig. 4. The data is displayed in various 2d projections in planes perpendicular to each other and well suitable to visualize the sample arrangement. A field-of-view of $(4 \, \text{mm})^2$ is used for all the projections (a)–(c). No phase correction was applied on the acquired data, and the absolute value of the signal strength is depicted in the maps. As described in the previous section, the crystal observed to be centered around (4 mm, 0, 0) is contacted along and oriented with long, highly conductive, axis parallel to the x-direction. The second object observed to be centered at about (3 mm, 1 mm, −1 mm) represents the smaller, non-contacted crystal.

3.2. Integral current analysis

In a first step, the integral value of the current dependent phase shift $\Delta\Phi$, averaged over the entire sample arrangement, was derived from the difference scheme shown in Fig. 1. The experiment was performed without pulsed gradients in order to achieve data for $k \equiv 0$. The resulting phase shift as function of I is shown in Fig. 5. For small I values one expects a linear dependence, with a straight line through the origin. Only for higher currents, in combi-

nation with the presence of nonuniform current distribution, one may expect a deviation from the proportional dependence [23]. The experimental data is in good agreement with this prediction and shows the expected linear slope for $-115 \, \text{mA} \leqslant I \leqslant 115 \, \text{mA}$. The slope, which is determined by the charge carrier density n, compares well with the theoretically predicted value, thus acknowledges the reliability of this newly introduced method [23]. Compared with an earlier examined crystal, the present phase shift is larger by a factor of two [23], indicating a smaller cross-section.

However, our stated aim in the present study is to obtain a spacial image of the current density, i.e. a position dependent current distribution map. To this end, the spatially encoding pulsed gradients have to be applied.

3.3. Current density imaging

In order to obtain current density images the pulse sequence described in Fig. 1 was fully implemented, including its spatial position encoding part. By stepping the pulsed gradients, a 9^2-matrix of the k_y,k_z-plane was achieved, and by Fourier-transform after zero-filling an ESR-image of 16^2-pixels was derived (Fig. 6a). Please note that in accordance with the pulse sequence shown in Fig. 1, and unlike the data acquisition used to obtain the projections shown in Fig. 4, this image has been generated without any read gradient, but with two phase encoding gradients in order to use the quasi-static gradient G_x for current encoding. Only the data point for $t = 2\tau$ has been analyzed for this picture. It shows the two-dimensional projection of the conduction electron spin density—again T_2 weighted—in the y,z-plane, namely perpendicular to the chosen current direction. The rather poor spatial resolution has been enforced by the S/N ratio required for phase determination for each individual pixel. However, the result is in good agreement with Fig. 4c showing the *same* projection of conduction electron spin density with better resolution.

In Fig. 6b and c, we present the main result of this study. The phase shift $\Delta\Phi$ for two different currents, of $I = 14 \, \text{mA}$ and $I = 45 \, \text{mA}$, was derived for each pixel in projections (b) and (c), respectively. We display in (b) and (c) only those pixels featured in Fig. 6a with 50% or more of the maximum signal intensity. The phase shift of the reference crystal, acquired with $I = 0$, defines the instrumental phase corresponding to $\Delta\Phi \equiv 0$.

The still rather inferior resolution of the phase contrast maps Fig. 6b and c does not yet allow a critical discussion of specific microscopic properties (e.g. meandering currents). These maps, however, encourage discussion of some potential possibilities. It was already concluded in previous sections above that the poorly resolved spin density map of Fig. 6a provides nevertheless a faithful representation of the spin density distribution.

Setting aside speculations, we should point out first of all what appears to be a nontrivial inconsistency within
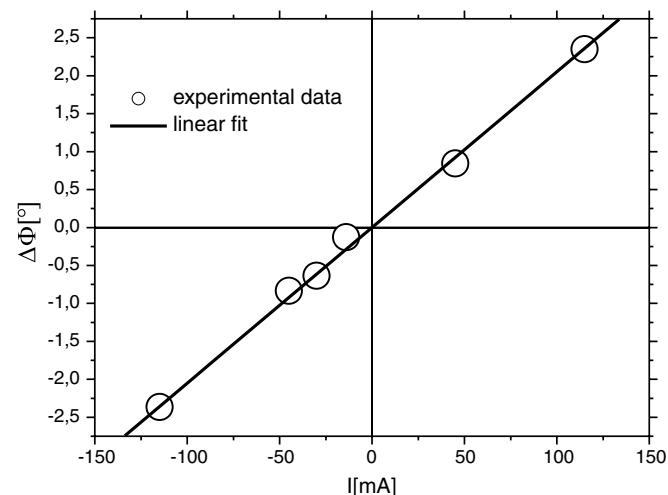

Fig. 5. Integral values of phase shift averaged over the entire sample. The solid line represents a linear fit, valid for small I values and describing the experimental data very well. See [23] for details.
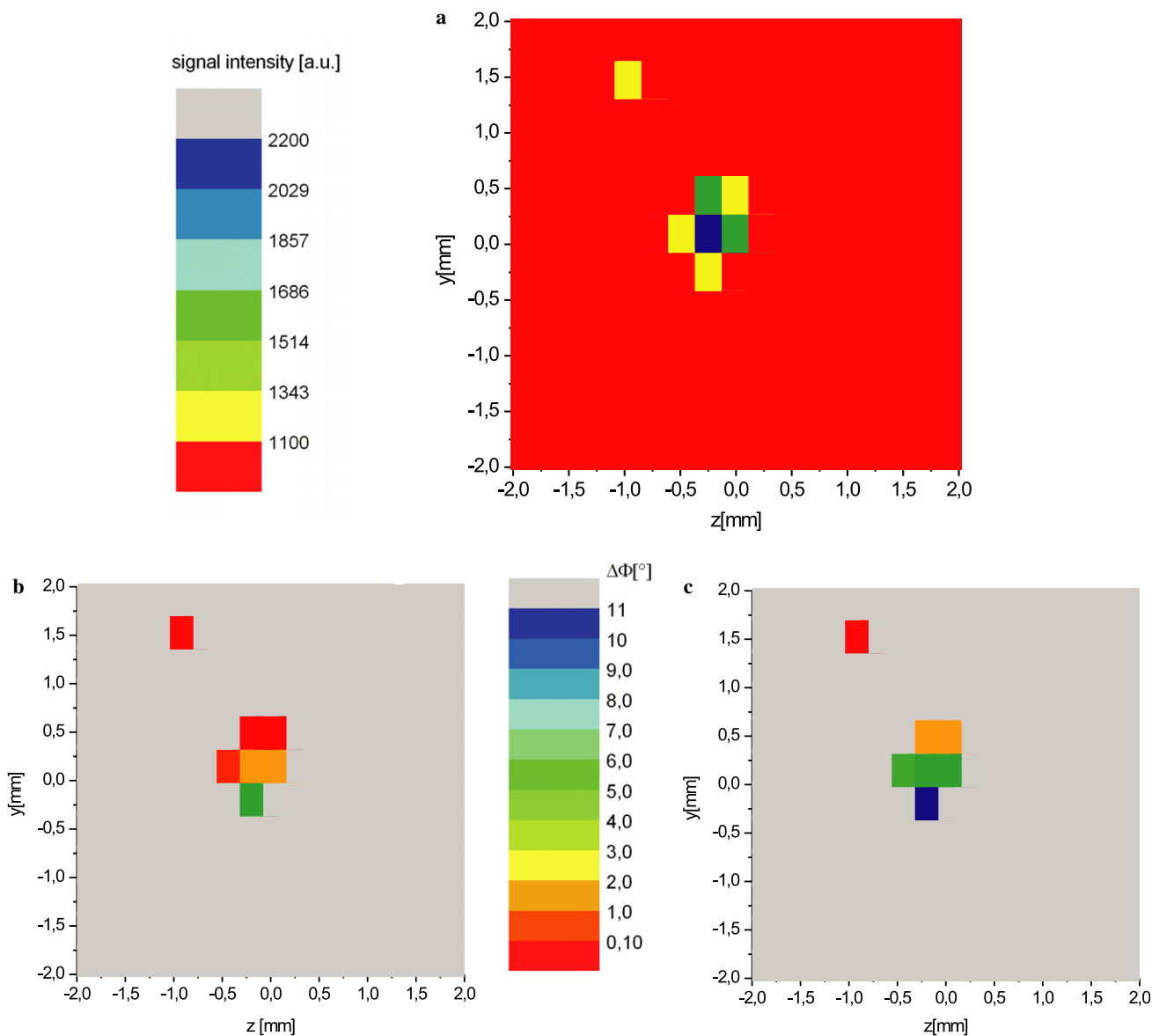
Fig. 6. (a) Two-dimensional projection of conduction electron spin density achieved by Fourier imaging using two pulsed phase encoding gradients. The field-of-view is identical to Fig. 4c, and in spite of the low resolution of 16^2 pixels in full qualitative agreement. (b and c) Spatially resolved phase shift $\Delta\Phi$ for currents perpendicular to the displayed plane of $I = 14$ mA and $I = 45$ mA, respectively. The non-contacted crystal is used as reference ($\Delta\Phi \equiv 0$). Pixel size: $240 \times 345 \ \mu m^2$.

the experimental results. By integration over the phase shift distribution maps (Fig. 6b and c) of the pixels with 50% or more of the maximum signal intensity in Fig. 6a, we find that the latter's (weighted) average is nearly by a factor of five larger (per given current). Since the integral phase shift analysis does not require the pulsed G_y and G_z gradients, the experiment is more robust and its numerical result is therefore expected to be more reliable. Therefore, until this discrepancy is removed, one has to be careful with absolute quantitative interpretation of current density distribution images.

However, it is reassuring also to note that the two phase maps withstand a self consistency test in that the ratio of the phase shifts of corresponding pixels in the two maps

scale roughly with the ratio of the currents quoted above. Thus, from a naive point of view, it may be somewhat surprising to find with many pixels a significant pixel by pixel *anti-correlation* between the phase shifts exhibited in maps (b and c) and the spin density distribution presented in map (a). For a physical speculation, we may note that for crystals of good quality (lower than 10^{-3} defects) T_2 increases and mobility decreases with defect content [24,25]. Thus, we 'understand' that pixels at the lower parts of the spin density map gives a weak signal, if it is of rather perfect quality and gives later rise to large current. That the same argument does not hold also for the upper right corner could be due to the contact area. The current density distribution could also reflect a real experimental situation of

non-uniform electric contact at either end of the sample, bearing in mind that the highly directional conductivity along the crystal axis may persist and propagate contact irregularities well into the crystal body. Finally, the current maps might be distorted by an artefact resulting indirectly from partial volume effects which tend to be significant in cases where a substantial number of the pixels is bordering the surface of the imaged object.

4. Conclusions

We demonstrated that it is in principle possible to visualize the non-uniform electrical current density distribution in solids using pulsed conduction electron spin resonance imaging techniques. We presented a pulse sequence scheme designed to eliminate spurious gradients induced by the current itself, as well as to provide spatial resolution. Therewith, an important step has been taken towards the fascinating goal of obtaining three-dimensional ESR images showing electronic current meandering through crystals.

In practice, almost all electrical transport phenomena involve electrons as charge carriers, and thus one cannot overemphasize the importance of the benefits to be had by developing this new technique further by means of resolution and applicability to other materials. Technical improvements in two major areas may contribute significantly for a more useful ESMRI system: (i) improved S/N and (ii) faster switching sequence controllers and pulsed magnetic field gradient drivers.

Acknowledgments

References

[1] B.C. Gilbert, M.J. Davies, D.M. Murphy (Eds.), Electron Paramagnetic Resonance, RSC, London, 2002.
[2] A. Blank, C.R. Dunnam, P.P. Borbat, J. Freed, J. Magn. Reson. 165 (2003) 116.
[3] M. Drescher, E. Dormann, Europhys. Lett. 67 (2004) 847.
[4] G.R. Eaton, S.S. Eaton, K. Ohno (Eds.), EPR Imaging and In Vivo EPR, CRC Press, Boca Raton, FL, 1991.
[5] G. Alexandrowicz, T. Tashma, A. Feintuch, A. Grayevsky, E. Dormann, N. Kaplan, Phys. Rev. Lett. 84 (2000) 2973.
[6] M. Drescher, N. Kaplan, E. Dormann, Phys. Rev. Lett. 94 (2005) 016404.
[7] C.L. Dumoulin, S.P. Souza, M.F. Walker, Magn. Reson. Med. 9 (1989) 139.
[8] R. Kimmich, NMR: Tomography, Diffusometry, Relaxometry, Springer, Heidelberg, 1997.
[9] E.L. Hahn, J. Geophys. Res. 65 (1960) 776.
[10] P.R. Moran, Magn. Reson. Imaging 1 (1982) 197.
[11] P.T. Callaghan, Principles of Nuclear Magnetic Resonance Microscopy, Oxford University Press, Oxford/New York, 1991.
[12] P.G. Morris, Nuclear Magnetic Resonance Imaging in Medicine and Biology, Clarendon Press, Oxford, 1986.
[13] P. Mansfield, P.K. Grannel, J. Phys. C6 (1973) L422.
[14] M. Glied, M. Drescher, E. Dormann, J. Magn. Reson. 180 (2006) 163.
[15] M. Conradi, A.N. Garroway, D.G. Cory, J. Miller, J. Magn. Reson. 94 (1991) 370.
[16] A. Feintuch, G. Alexandrowicz, T. Tashma, Y. Boasson, A. Grayevsky, N. Kaplan, J. Magn. Res. 142 (1999) 382.
[17] M. Drescher, Austr. J. Chem. (2005).
[18] G.G. Maresch, A. Grupp, M. Mehring, J.U. von Schütz, H.C. Wolf, J. Phys. I 46 (1985) 461.
[19] M. Mehring, Low Dimensional Conductors and Superconductors, in: D. Jerome, L.G. Caron (Eds.), Plenum, New York, 1987, p. 185.
[20] H.C. Torrey, Phys. Rev. 104 (1956) 563.
[21] T. Wokrina, J. Gmeiner, N. Kaplan, E. Dormann, Eur. Phys. J. B 35 (2003) 191.
[22] U. Köbler, J. Gmeiner, E. Dormann, J. Magn. Magn. Mater. 69 (1987) 189.
[23] M. Drescher, N. Kaplan, E. Dormann, Phys. Rev. Lett. 96 (2006) 037601.
[24] J.M. Delrieu, M. Benguin, M. Sanquer, Synthetic Metals 19 (1987) 361.
[25] T. Tashma, A. Feintuch, A. Grayevsky, J. Gmeiner, A. Gabay, E. Dormann, N. Kaplan, Synthetic Metals 132 (2003) 161.